Available online at www.sciencedirect.com

SCIENCE DIRECT®

Cement and Concrete Research 36 (2006) 896 – 911

Cement and Concrete Research

Confocal imaging of porosity in hardened concrete

M.K. Head *, N.R. Buenfeld

Concrete Durability Group, Department of Civil and Environmental Engineering, Imperial College London, SW7 2BU, UK

Received 25 November 2004; accepted 6 June 2005

Abstract

We present the results of an exploratory 3D study of fine pore structures in hardened cement paste. A laser scanning confocal microscope was used in reflected (epi) fluorescent imaging mode, allowing for the very high optical resolution of features well below 1 μm in size. Images of pore structures were captured using a 'reverse imaging contrast' technique where spaces in the material were impregnated with a fluorescent, dyed epoxy-resin, and scanned in the $x-y$ plane by a laser probe. A vertical 'stack' of these optical sections was acquired by imaging sequentially through the z-axis. Using this technique it was possible to observe, partially hydrated cement grains, porous natural quartz aggregate interfaces, micro-cracking in the hydrated cement paste and aggregate particles, as well as fine capillary pores and very small air voids. Operating at the limit of its capability the microscope was able to perform high resolution imaging of the internal areas of partially reacted cement grains, and pore structures approximately 0.17 μm across were measured. 3D models were produced to help visualise the true morphology and distribution of porous features.

Keywords: 3D Laser Scanning Confocal Microscopy (LSCM); Characterisation; Petrography; Backscattered Electron Imaging

1. Introduction

Size, distribution and connectivity of the pore space is of paramount importance to the durability related properties of hardened concrete, due to the ability of fluids and ions to move through connected pore networks. Much information relating to the distribution and micro-structural nature of voids and phases has been gained by analysing micrographs captured with scanning electron microscopes (SEM) and, to a lesser extent, optical micrographs, of polished blocks and thin sections. This information however is limited to a two-dimensional (2D) plane, meaning that stereological modelling is required to compensate for the lack of data relating to the three-dimensional (3D) nature of the material. It is therefore very important to develop techniques that are able to image and accurately reconstruct the 3D micro-structure of hardened concrete.

This paper will present a 3D optical technique not previously applied to the 3D study of pores and voids in HCP or concrete. Confocal microscopy is well established in the biosciences as a tool for imaging and reconstructing cells, organic tissue, and microscopic organisms. Tagging of different molecules with different fluorescent markers allows multi-channel image capture to be performed resulting in vivid, in-focus images of object structures. In the geological sciences, confocal imaging has recently been used for examining pores and pore networks in hydrocarbon reservoir rocks and sandstones [1–3], and also for understanding crack formation in harder rocks such as granite [4].

In the field of cementitious construction materials however, the confocal technique is new and under-developed with only relatively cursory investigations of fracture surfaces, hydration products, and aggregate interfaces [5–8]. To the authors' knowledge, there have not been any previous studies that have applied confocal microscopy to the examination of pore structures present in cement-based materials. Neither have there been any previously published applications of fluorescent imaging in the confocal micro-

---

* Corresponding author. Tel.: +44 207 594 5956; fax: +44 207 225 2716.
E-mail address: m.head@imperial.ac.uk (M.K. Head).

0008-8846/$ - see front matter © 2005 Elsevier Ltd. All rights reserved.
doi:10.1016/j.cemconres.2005.06.006

scope to cement-based materials. The objectives of this study were to establish whether the fluorescent confocal technique could be used to image the 3D pore structure of hardened cement-based materials, and to assess the depth of material that can be probed.

2. Specimens

Two specimens of hardened mortar were dried at 50 °C for 3 days and then vacuum impregnated with an araldite type epoxy resin that had been stained with a fluorescent yellow dye. 5% Toluene was added to the resin/hardener mix to help reduce the viscosity during impregnation. The dye had been mixed by machine into the resin part only, for at least 3 days prior to this to prevent any 'clumping'. Mortar 'A' comprised of a binder : aggregate : water ratio of 1 : 4.8 : 0.70, and mortar 'B' comprised of a binder : aggregate : water ratio of 1 : 2.97 : 0.35. The dried concrete samples were placed in a sealed vacuum chamber and evacuated to remove air from pores and voids. The mixed resin was out-gassed in the same chamber before being poured over the specimens while still under vacuum. Impregnation of the specimens was achieved by cycling of first chamber evacuation and then slow release of the vacuum. This helps to reduce the likelihood of damage to the microstructure, and helps to drive the resin into finer pores [9,10].

After the resin had hardened, the specimens were lapped with a 9 μm aluminium oxide (Al_2O_3) powder. The new surface was re-vacuum impregnated with the low-viscosity dyed-resin (with repeated vacuum release cycles), and again lapped with the Al_2O_3 powder so that an impregnated surface layer of about 100–200 μm remained. This surface was bonded to a 50 × 75 mm glass slide using the same epoxy resin with no added fluorescent dye. Both specimens were then thinned by a cut-off saw and lapped so that the impregnated layers remaining on the slides achieved a final thickness of approximately 30 μm (illustrated in Fig. 1).

a) Mortar A– 0.70 w/c

b) Mortar B – 0.35 w/c

Fig. 1. Scanned images of the specimen thin sections (areas ~40 × 60 mm).

The surfaces were polished with progressively finer diamond polishing pastes, with the final particle size being 1 μm, for use in reflected light mode and backscattered electron (BSE) imaging in a SEM. A polished surface causes a cleaner backscattered electron signal to be detected; it also causes less diffraction of light from sub-surface image planes than, for example, a surface finished by lapping, thereby improving confocal signal detection. The thin sections for each mortar were scanned into a computer using a high resolution slide-film scanner, the images to be used later as 'maps' to relocate areas analysed.

3. Instruments

The confocal microscope used in this study was a Zeiss LSM 510 mounted on a Zeiss Axioplan2 upright microscope. The microscope was also fitted with a standard fluorescence imaging system, and, polarising filters for use in transmitted and reflected light. Images captured with a confocal microscope can be formed in essentially two light modes, visible (white) light and fluorescent light. By scanning the light source (in this case a laser) across the specimen, it is possible to build up an image of the specimen that is spatially resolved to <0.2 μm. If the specimen is also imaged sequentially through the vertical '*z*' axis, the resulting image 'stack' can be reconstructed as a model in virtual 3D space. A very small pinhole aperture is placed directly in front of a light detector (a photomultiplier tube, or PMT), in a plane that is conjugate to the focal plane of the specimen objective lens, hence the term 'confocal'. In this position the aperture is able to block most of the light that is not in focus, and only light that is in sharp focus is allowed to pass un-restricted through the pinhole to the detector to form an image. This is illustrated by the beam path diagram in Fig. 2.

Light that originates from a point above the focal plane (represented by the dotted line) comes to a focus above the pinhole aperture, and light originating from below the focal plane (represented by the dashed line) comes to a focus below the pinhole aperture. In both cases most of this light is unable to pass through the aperture to the detector. By varying the diameter of the pinhole (which is infinitely adjustable from closed to a size larger than the light ray bundle), the thickness of the optical slice can be adjusted allowing optimisation of vertical resolution. For a given depth of focus, smaller pinhole diameters will require larger

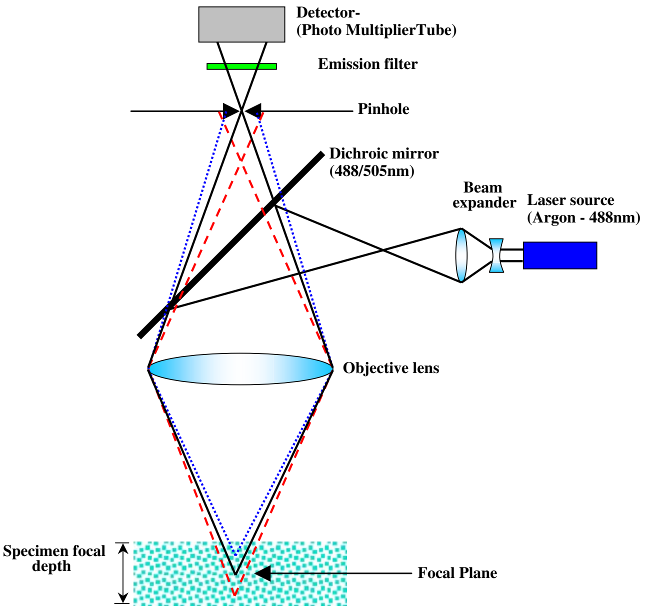

Fig. 2. Diagrammatic representation of the confocal principle.

numbers of optical slices or sections to be captured, and at closer intervals.

The resolution of the confocal microscope is affected by several different factors. The most important component in the system is the objective lens and its light gathering capability, and in this work, a Plan-Apochromat ×63 oil immersion lens with a numerical aperture (NA) of 1.4 was used. This lens also acts as a condenser lens in reflected light mode. The wavelength of light also influences resolution, where shorter wavelengths provide better resolutions than longer wavelengths. The resolving power of the microscope used in this study is about 0.18 μm for a pinhole aperture setting greater than or equal to one Airy Unit[1] (AU). For a pinhole setting less than 0.25 AU, this becomes ∼0.13 μm. The best axial (vertical) resolution is about 0.3 μm for a pinhole smaller than 0.25 AU.

Fluorescent imaging of pores and other spaces in hardened cement paste (HCP) relies on the premise that the dyed resin is able to penetrate into them, and when irradiated by a high energy light source produces a fluorescent luminosity that is detected by the system's camera, or detector. This has allowed conventional fluorescent microscopy to be developed as a method to estimate the original w/c of hardened concrete, by comparing specimen luminosity with pre-fabricated specimens of known w/c [11–14]. Conventional fluorescent microscopy is able to image coarse features such as air voids and cracks, but not capillary pores as they are too small to be resolved by such systems, i.e., they image *total fluorescent luminosity* and *not individually resolved capillary pores*. Instead, the HCP appears luminous and highly contrasted against the non-impregnated aggregate particles and other opaque phases such as unreacted cement grains. Fig. 3 is a conventional non-processed fluorescent micrograph of a test area of mortar B, captured with an Olympus BX51 petrographic microscope, equipped with a reflected fluorescent light illuminator and filter set. The set-up matches the excitation and emission wavelengths used in the confocal microscope allowing the same specimens to be examined in both instruments.

The image shows various areas of porosity within the HCP, a porous aggregate particle in the lower left quadrant and numerous other low porosity aggregate particles. A few small air voids can also be observed (for example, in the top left corner marked with a 'v'). The image area was also analysed during an earlier test run with the confocal microscope, and an area of darker shadowing within the HCP can be observed in the centre of the image. This is photo-bleaching of the dyed resin, which was caused by experimental operation of the laser at 100% power. Subsequent tests confirmed that the laser could be operated at power levels as low as 25% with no observable photo-bleaching or degradation of signal quality.

To confirm the identification of images formed by the confocal microscope, test areas of the 0.70 w/c mortar were imaged by confocal fluorescence, and then by BSE imaging in a JEOL 5410LV SEM. Partially reacted cement grains were first selected for imaging with the confocal microscope, and their positions were marked on hard copies of the scanned sections shown in Fig. 1. A low magnification BSE image (×50) of the general area where the grains were located was captured to show their relative position, and, the overall appearance of the mortar microstructure. This is presented in Fig. 4, along with BSE images of both locations captured at the same scale as the confocal images.

It can be seen that the 2D resolution of fluorescent confocal micrographs is comparable to resolutions obtained

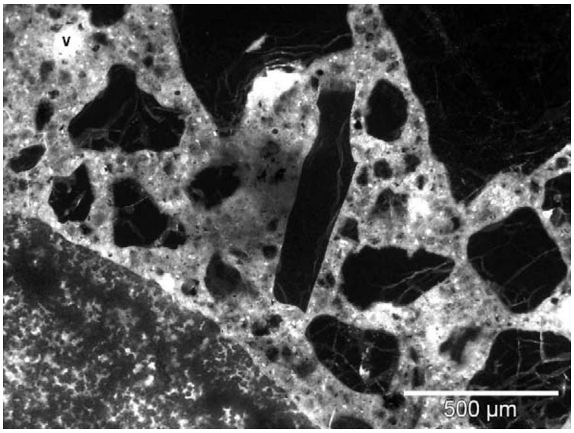

Fig. 3. Conventional reflected fluorescence micrograph of a test area of mortar B (0.35 w/c), large void marked 'V'.

---

[1] An Airy Unit describes the dimensions of a diffraction pattern of light rays, originating from a point source, as they pass through a diffracting medium. The pattern is observed as a series of concentric rings around a central maximum intensity disc known as an Airy Disc, with intensity decreasing away from a central point. This unit is used to calculate ultimate resolutions of diffraction based instruments such as optical microscopes.

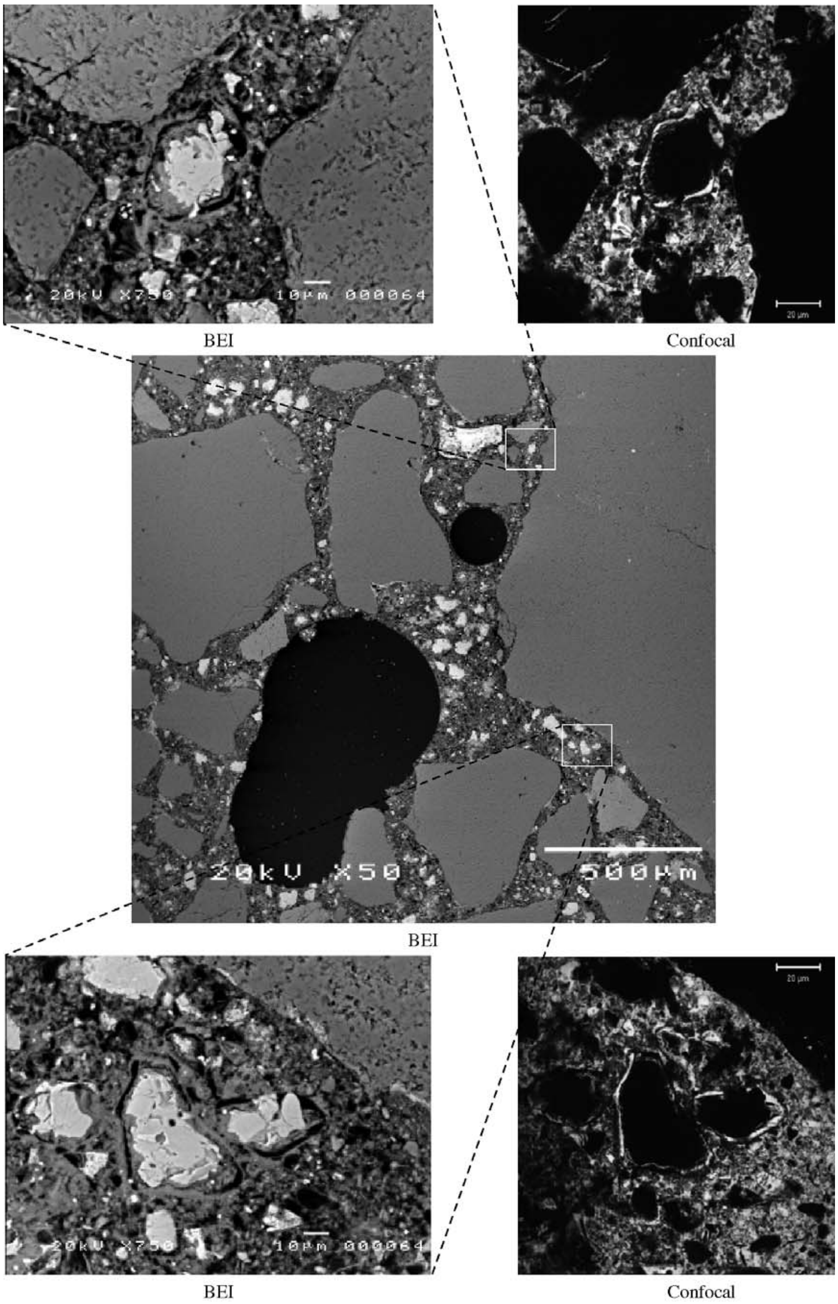

Fig. 4. Matching confocal image areas with backscattered electron images (mortar A — 0.70 w/c).

with an SEM, and is a characteristic that may be exploited in future work. However, the comparison of BSE with confocal images highlights the inability of this particular confocal technique to discriminate different solid phases of the material, and should be considered if all fractions of the hardened micro-structure are to be examined.

4. Image *z*-stack acquisition

To form an image *z*-stack from detected fluorescent light, light excited by the laser probe must be detected from points on or below the specimen surface. The semi-transparent nature of very thin wafers of HCP makes this possible, and it is for the same reason that thin sections of hardened concrete are preferred by concrete petrographers. These specimens can be made thin enough to reduce much of the scattering and diffraction effects suffered by light, as it passes through multiple particles that overlie each other through the thickness of the section. However, even when imaging with a laser scanning confocal microscope (LSCM), a gradual loss of signal with depth can be expected as light is progressively unable to penetrate the material in order to excite the fluorescent dye. The signal produced from a probed spot becomes weaker and eventually indistinguishable from the background noise. Given this gradual reduction in the

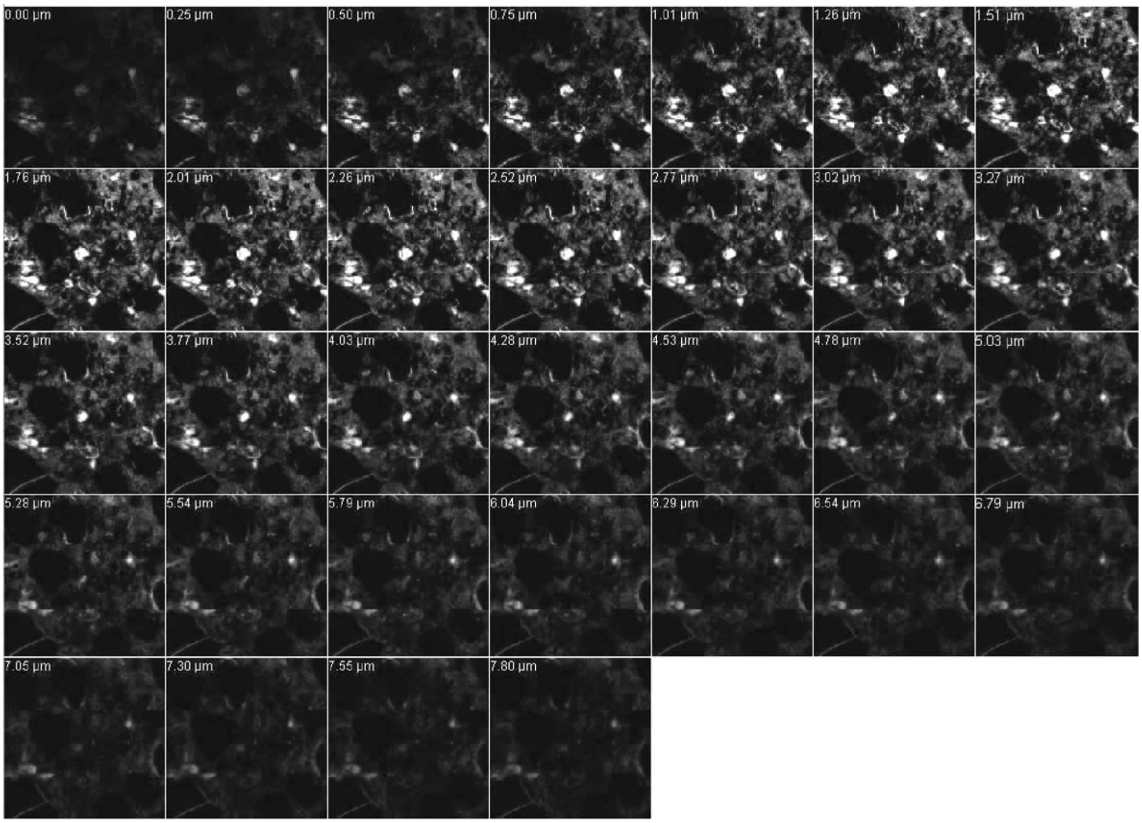

a) Without signal loss compensation

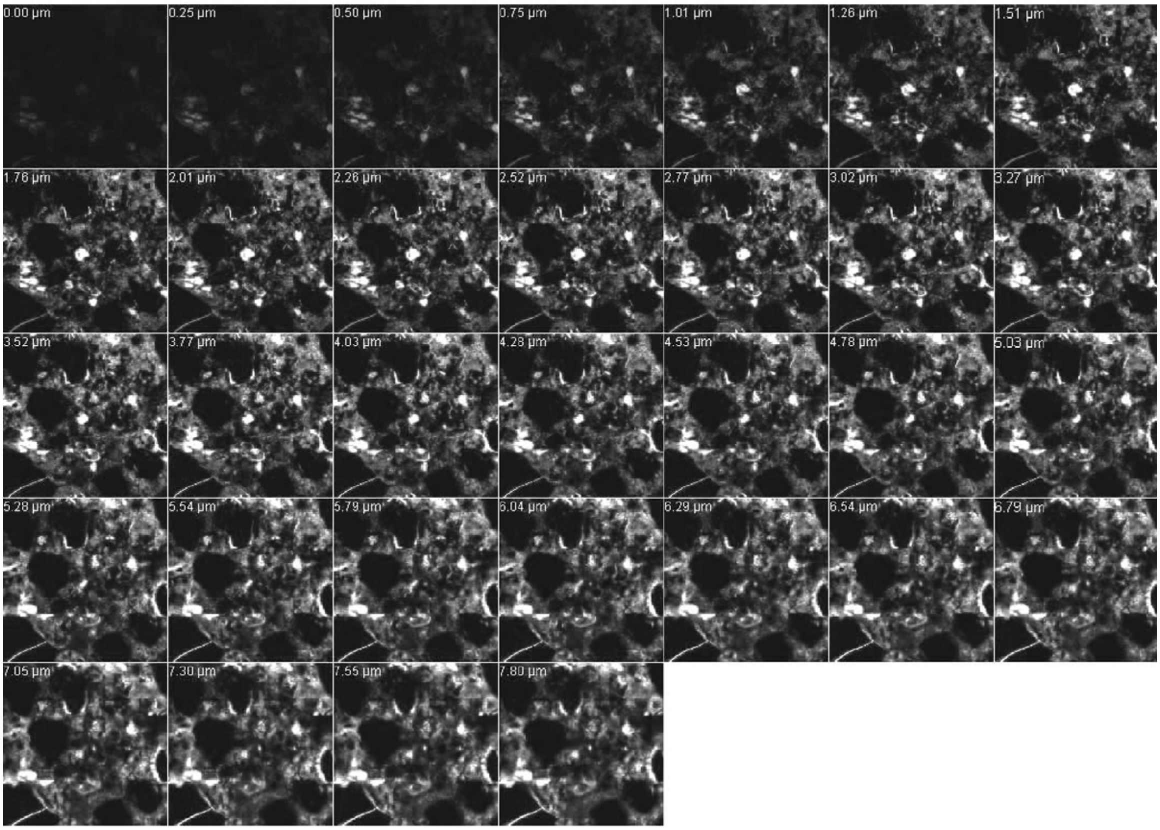

b) With signal loss compensation

Fig. 5. Screen shots of confocal z-stack galleries of the same area of mortar B imaged through 7.8 µm of depth.

detected signal, the resolution of features with depth therefore becomes increasingly poor.

The LSM 510 is able to capture image data sets automatically according to preset criteria. The start and finish positions for the *z*-stack were set respectively at the top and bottom of the focal depth to be imaged. Then, the total number of *z*-stack 'image slices', optical slice thickness (controlled by pinhole size), optical slice interval and overlap, *z*-stack auto-brightness compensation (see below), any preset digital zoom factor, and any preset averaging of detected signals were set according to the unique conditions of individual test areas. When image capture commenced, the specimen was automatically moved so that the top (start) position of the specimen was positioned in the focal plane, and the first image in the stack was captured. The stage was then moved up so that the next image slice was captured at a deeper depth within the specimen than the previous slice, and so on, until the stack was complete. The data was then saved as a digitised *z*-stack file in proprietary format.

This particular instrument is able to auto-compensate (to a certain degree) for signal loss with depth, by auto-adjustment of the detector sensitivity (gain and offset). Fig. 5 shows two complete image galleries captured from the same, arbitrary area of mortar B (0.35 w/c), and demonstrates the effect of signal loss and of signal loss compensation.

For the non-compensated data set (Fig. 5 a)), it can be seen that at depth 0 (the specimen surface) a low intensity value is recorded for the fluorescent signal received from surface features just touching the focal plane, and the image is generally dark. As the focal plane depth is increased the signal increases, and the image appears brighter as more voids filled with fluorescent resin are encountered. This increase continues to a depth of approximately 2 μm (maximum intensity), after which the signal starts to decrease until a depth of approximately 8 μm is reached and imaging was stopped. At this depth, much of the signal is lost and few features can be easily recognised. In Fig. 5 b) however, intensity is maintained by auto-compensation throughout the imaging depth, and the brightness of images is retained even after the maximum intensity depth is reached. Fig. 6 is a plot of mean fluorescent intensities for each frame of the two image data sets shown in Fig. 5. The two intensity curves have been labelled 'a' for Fig. 5 a) and 'b' for Fig. 5 b), to correspond to each image gallery.

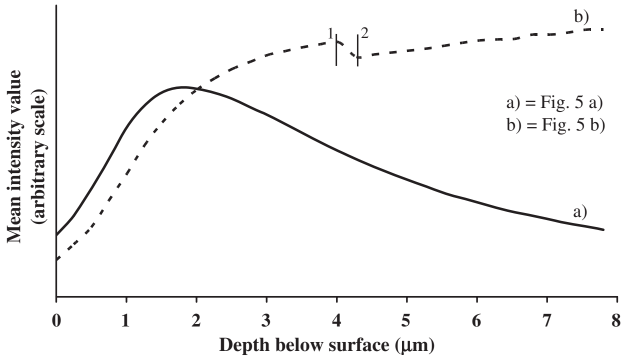

Fig. 6. Intensity profiles for signal loss auto-compensation (line 1 marks beginning of signal loss, line 2 marks point at which compensation begins).

For both data sets the intensity profile trend is similar over the first 2 μm, although a slight calibration difference has resulted in a lower initial intensity value at depth 0 for curve 'b' (compensated data set). The depth imaged for this data set, before signal loss is observed, is approximately 4 μm and is due to the increased sensitivity of the detector. After 4 μm a small step in the curve is visible (marked by lines '1' and '2'), marking the point at which the detected signal begins to weaken (line '1'), prior to initiation of detector sensitivity auto-compensation (line '2'). The effect after this point is that the intensity profile does not tail-off as for curve 'a' (non-compensated data set), but remains near constant to the chosen maximum imaging depth of approximately 8 μm, resulting in the clearer images shown in Fig. 5 b). Images and feature resolution will inevitably suffer from amplified noise with increased depth, but the signal received is sufficiently 'clean' to allow feature reconstruction over the same *z*-axis distance as before. Ideally the system would be calibrated such that the compensated signal initiates at line '1' in curve 'a', and produces a smoothed constant signal to the maximum image depth without any step in the intensity curve. In the above case, a slight dark banding will be apparent at approximately 4–5 μm depth if the *z*-stack of images is viewed in profile (*x* or *y*).

5. Image processing

Image processing was carried out post-capture on all confocal data sets. This is necessary to ensure that as clean an image as possible is available for examination and quantification. The objective of processing 3D confocal data is to produce a 3D model that is as complete as possible and is as true to the real structure of imaged features as possible. This begins with the best adjustment of the imaging system during image capture and includes optimising resolution and image formation steps as previous, plus, averaging of data capture to remove unwanted signal noise. Satisfactory data sets can then be re-processed with a large variety of available preset and custom designed image filters.

All optical systems suffer from a phenomenon known as 'lens flare' or diffraction of a point light source through a medium which possesses a refractive index. This is known as the 'point spread function' (psf) of the system and is specific to the optical properties of individual imaging systems. Light from a point source passing through an optical system would ideally produce a true image point or spot, however, the light experiences a certain degree of spread and the spot is therefore slightly blurred when imaged. The psf is a property of light optics that has been extensively studied, particularly in the sciences of bio-chemistry and bio-molecular engineering, which make wide

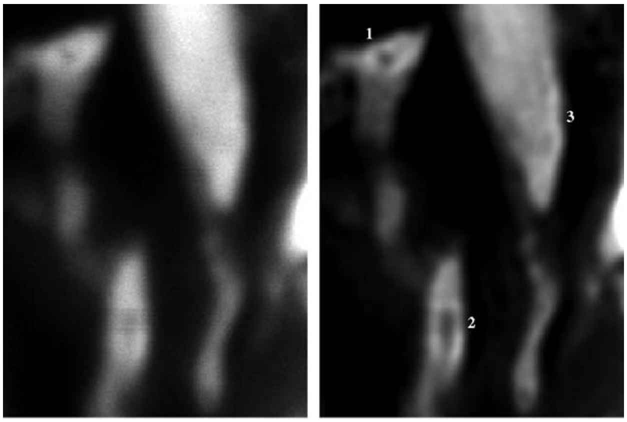

a) Pre image processing b) Post image processing

Fig. 7. Zoomed and cropped area of high-resolution confocal micrograph to demonstrate effect of image processing with low-pass, and then iterative deconvolution filters.

use of fluorescence and confocal microscopy with both single and multi-channel illumination imaging systems. Recent work in the field of biological deep 3D imaging by de Monvel at al [15] has attempted to improve the resolution of images by extracting the psf from the images themselves and is similar to research in astronomy that utilises light from a very distant star (i.e., a tiny point light source) to define the psf of the telescope system used. The work performed by de Monvel's team describes how small beads of sub-resolution size are often used to calculate the psf, but that a drawback is that they cannot accurately reproduce the actual imaging conditions of the image-capture sessions themselves. The results of the work confirm that this technique does produce images of a marked improvement over the system-idealised psf deconvolved images, and could be investigated further for processing of confocal images of pores in cementitious materials. This is the

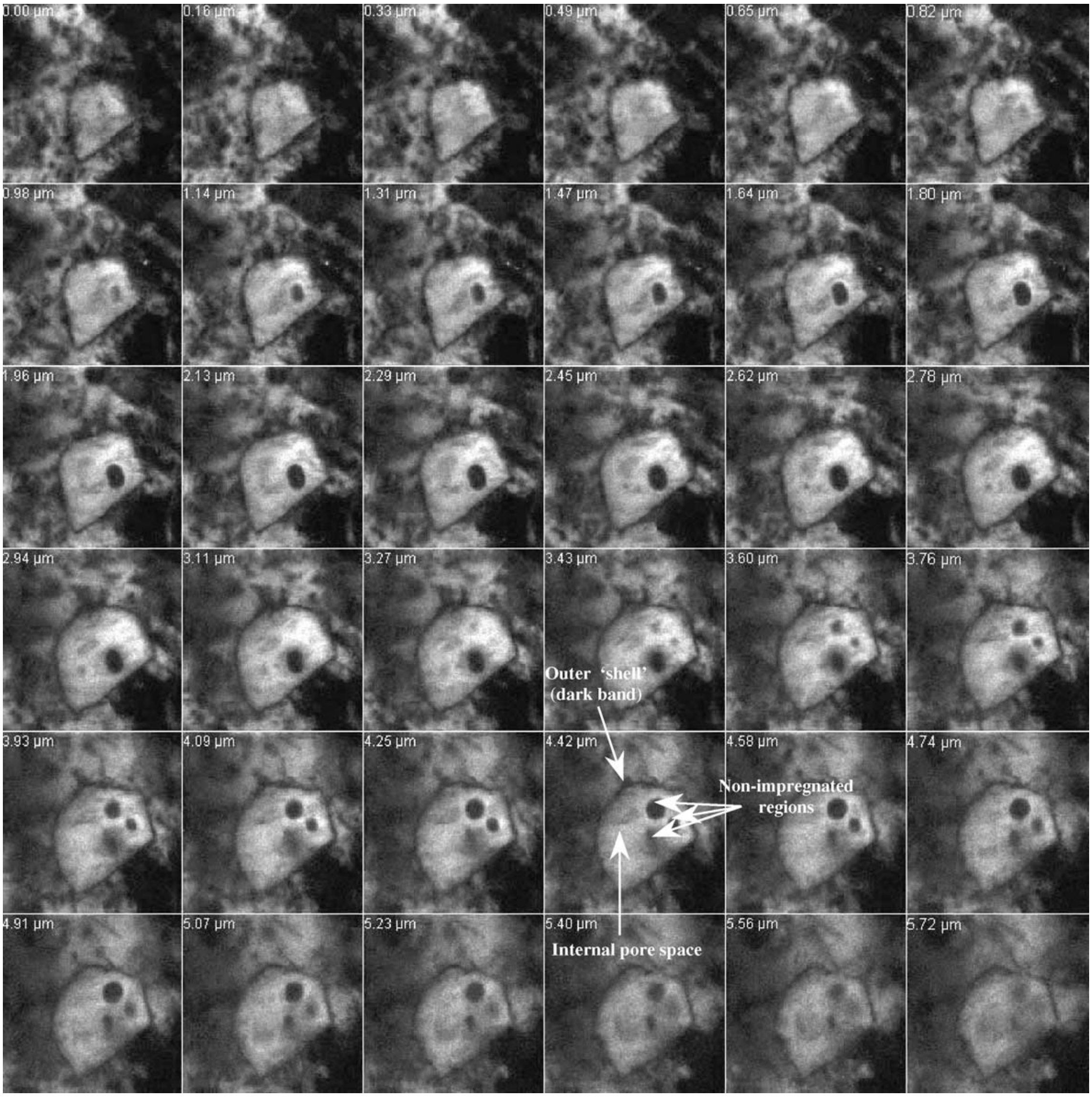

Fig. 8. Z-stack image gallery through 5.72 µm of almost fully reacted grain, mortar A — 0.70 w/c, FOV ~22 µm.Outer C–S–H shell, internal pore space and non-impregnated regions marked at z-axis depth of 4.42 µm.

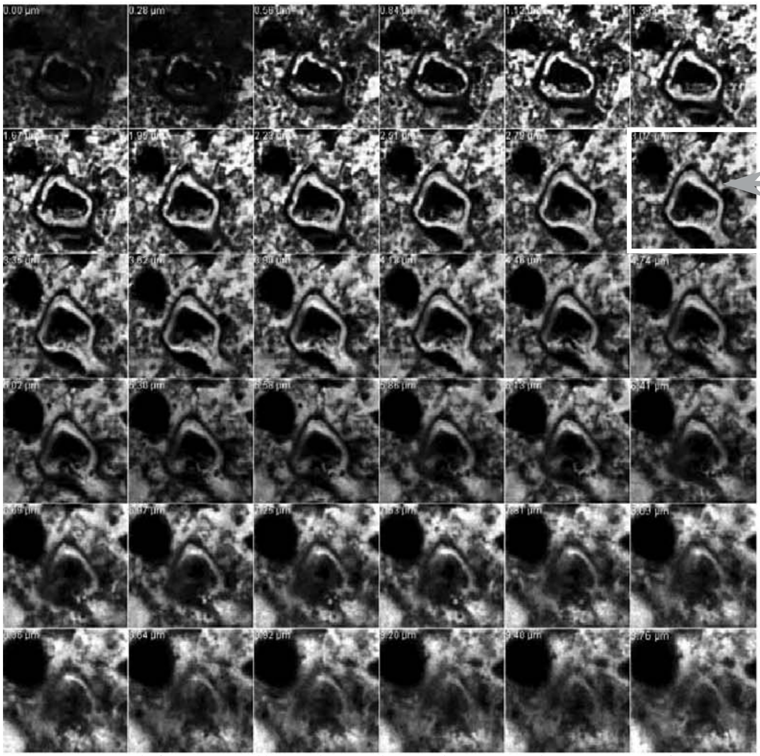

a) Z-stack image gallery through partly reacted cement grain. Connecting 'neck' observed from approx. 2.51 µm to 6.41 µm of depth.

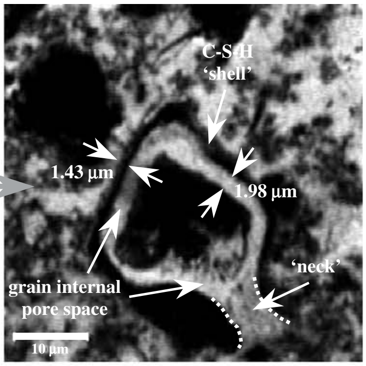

b) Frame 12 from image gallery.

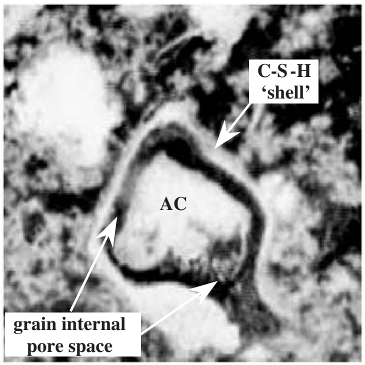

c) Inverted greyscale image of b). **AC** = anhydrous core.

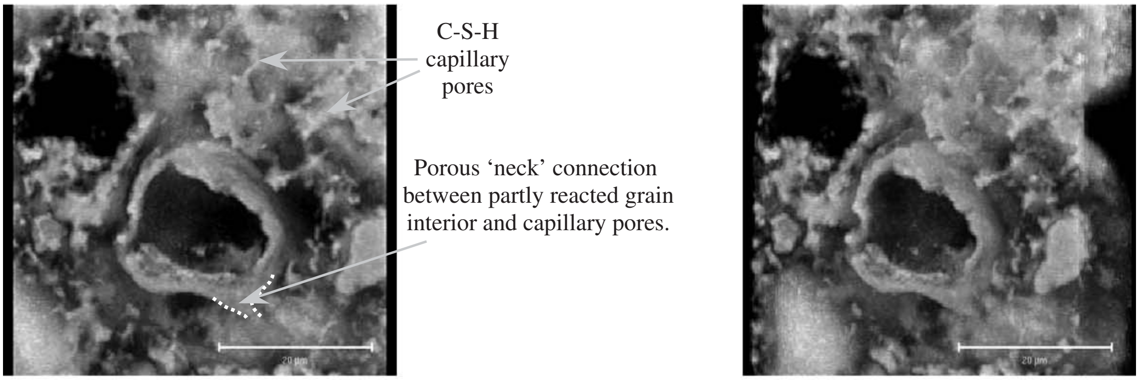

y axis rotation = 0° y axis rotation = 30°

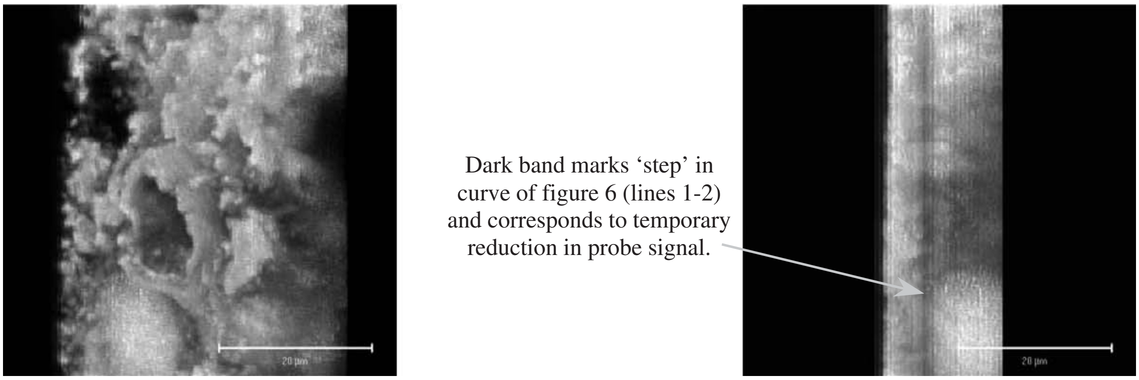

y axis rotation = 60° y axis rotation = 90°

d) Reconstructions of 3D data about y-axis organised at 30° intervals (scale bars = 20 µm).

Fig. 9. Image data set through a partly reacted cement grain (mortar A — 0.70 w/c).

subject of future work however and is not covered further here. Most confocal software incorporate deconvolution algorithms that are based around knowledge of the imaging system's psf, and data sets are normally captured with details of the microscope settings (pinhole size in airy units, emission wavelengths etc.) so that deconvolution can be carried out at later stages. Fig. 7 shows the result of basic image processing with a low-pass averaging filter, and then with an iterative deconvolution filter (included in the microscope's own software), which calculates the psf of the optical system based on image capture conditions.

These cropped images are taken from the high-resolution micrograph depicted in Fig. 11, and show the region of the micrograph used to measure fine detail. In a), feature structures are vaguely visible within some of the porous regions, but are generally obscured or blurred by the spread of light through the imaging system's optics (lens flare). In the processed image b), the same region clearly reveals finer details in areas where previously there appeared to be none. Not only have small porous conduits been separated (1 and 2), but also very subtle, fine details can now be observed in the larger porous region labelled '3'. Having said this however, processing should be kept to a minimum wherever possible, to preserve the data as near as possible to their original condition. Over-processing runs the risk of degrading image data such that features become idealised or even fragmented, instead of providing a faithful representation of the object investigated. Also the 3D images, presented here in 2D, are best viewed on a computer monitor where display resolutions are higher and the images can be rotated for viewing from different perspectives.

6. Pore structures imaged

Fig. 8 shows a series of 36 images captured from the 0.70 w/c specimen 'A'. The *z*-stack image-gallery covers an imaging depth of 5.72 μm through an almost fully reacted cement grain, which was captured at a total magnification of ×4158 (includes a digital scan zoom of ×6.6), and a pinhole size equivalent to ~0.26 AU.

The data set shows a thin dark line surrounding the fluorescent interior pore space of a reacted cement grain. This is interpreted as a 'solid' shell, into which fluorescent resin has entered to fill the interior void. Within this void there are a few small rounded dark regions that are clearly

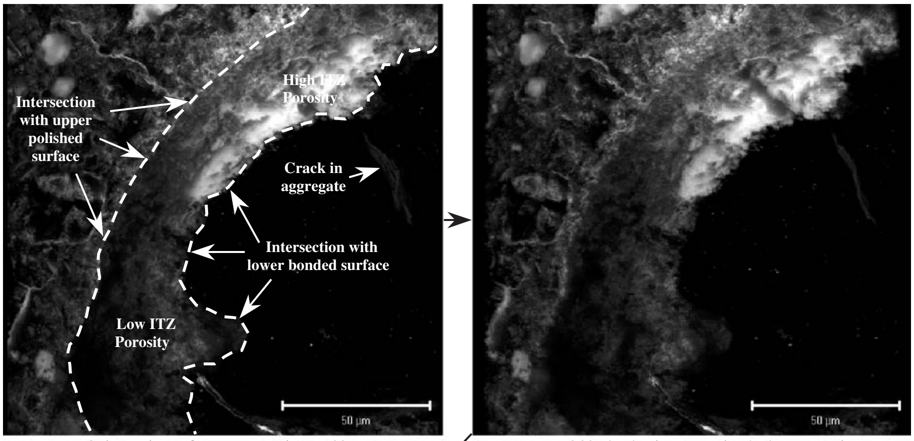

Orientation of reconstruction = 0º

30º clockwise 'rotation' about y axis

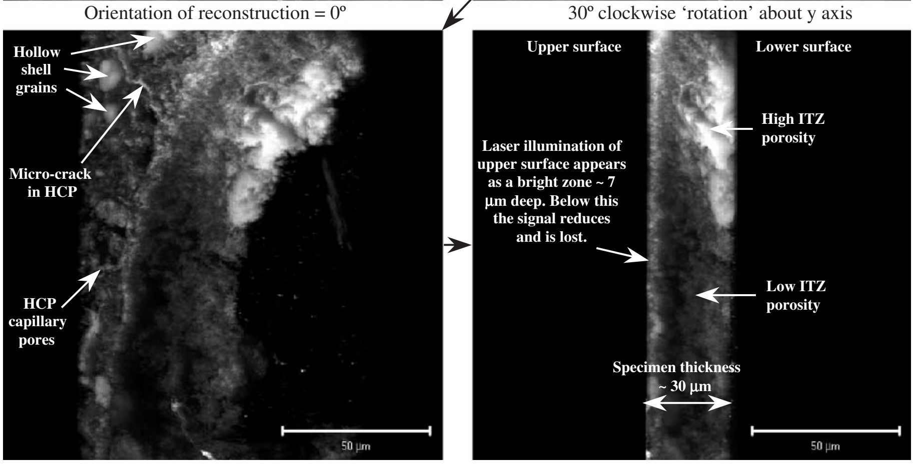

60º clockwise 'rotation' about y axis

90º clockwise 'rotation' about y axis

Fig. 10. 3D reconstructions of a natural aggregate interface, again at 30° intervals about the *y* axis, so that the fourth view is of the data set as viewed from the right of the first image. Scale bars = 50 μm (mortar B — 0.35 w/c).

separated from other features. These may be interpreted in turn as un-reacted phases/particles or trapped air bubbles, and it is possible to observe at least three within the original grain boundary. The gallery shows how all three particles first appear and then disappear as the imaging plane moves down through the object.

The following set of images (Fig. 9) show another reacted cement grain particle, but this time a different set of features can be observed. The gallery of images in a) show a partially reacted cement grain imaged through about 10 μm of its thickness. The images clearly show a dark outer 'layer' interpreted as an outer C–S–H shell (marked on Fig. 9 b)), which is even more prominent than the previous example, inside of which a reacted 'zone' (continuous lighter band) appears to have developed into internal pore space (also marked on Fig. 9 b)). This is surrounding a largely un-reacted core. However at a depth of around 2.5 μm, a connecting 'neck' (marked with dotted lines) appears to develop, which is clearly connected to the surrounding HCP porosity. In the region where the connection is in contact with the inner un-reacted core, very fine fibril-like pores have developed that presumably indicate the initial reaction of the core with free water present in HCP capillary pores. Fig. 9 b) has been converted to greyscale and inverted and can be observed in Fig. 9 c). This image appears more similar to images obtained from backscattered imaging, and has been included to aid interpretation of the other images of Fig. 9.

This connecting 'neck' structure is an important discovery given the unknown connectivity of 'hollow-shell' cement grains, or partly reacted cement grains, with HCP capillary pores. If the structure were to be observed on the specimen surface it is possible that it could be interpreted as an artefact of specimen preparation and discounted as such. The fact that it does not, and can be seen to develop as a structure with depth into the material, is evidence of an

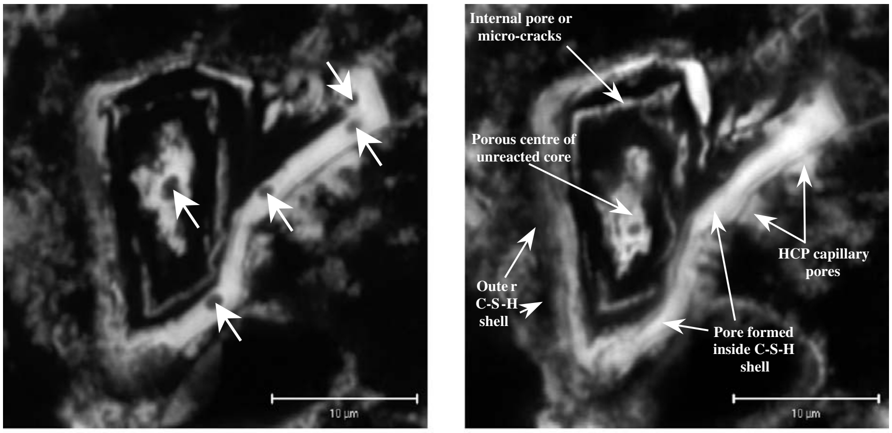

a) Image of partly reacted cement grain. (Digital zoom x5, total magnification x3150). Scale bar = 10 μm. Focal depth ~ 2.2 μm. Small, 'unreacted' regions marked with arrows.

b) Image plane deeper within grain (~ 3.5 μm) showing fine internal voids. Note unreacted 'particles' no longer present.

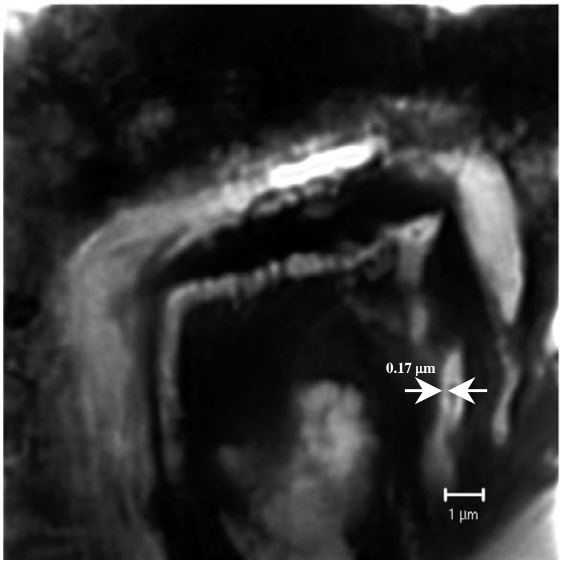

c) Region of b) with x10 digital zoom (total magnification = x6300).

Fig. 11. Partly reacted cement particle showing apparent symmetry of reacted areas (mortar B — 0.35 w/c).

independent development of the connection. If another part of the grain were also found to be independently connected to capillary pores, it would form a conduit allowing fluid/ion transfer to bypass HCP capillary pores, directly affecting transport properties of the material. The reconstructed 3D images shown in Fig. 9 d) show the general morphology of the grain, along with very fine features of HCP capillary porosity as viewed from 4 different 'rotated' angles. The 90° image can be seen to have a dark band running parallel to the image plane (x–y), which corresponds to the step in curve b) of Fig. 6.

The ability of the technique to image through a particle of natural clear-quartz sand aggregate revealing interfacial zone porosity is demonstrated in Fig. 10. The aggregate/cement paste interface is slightly concave and inclined from top left to bottom right, as viewed on the 3D reconstructed 0° rotational view. An increase in porosity can be observed towards the lower bonded surface (bonded to the glass substrate), as depicted by areas of higher intensity luminosity in the top right quadrant of the image.

For this data set the pinhole size was set at 1 AU with a line scan average of 4. Total depth imaged through the aggregate particle was measured at 30.9 μm, and z-stack auto-compensation was not used. The upper part of the HCP can be observed with a few reacted grains, a micro crack and other voids and pores also visible. This upper HCP zone appears as the thin bright line on the left side of the 90° rotated view and covers an imaging depth of about 7 μm. Below this, a signal was not detected.

When compared to other conventional optical imaging techniques, the lateral resolution of confocal microscopy is significantly better. To demonstrate this, Fig. 11 a) is a confocal fluorescent micrograph of another partly reacted cement grain. The grain appears to show concentric reaction zones or cracks surrounding a largely reacted core. The centre of the grain has almost fully reacted to leave a hollow space that was in-filled by fluorescent resin during impregnation. Similar patterns were observed in other partly reacted grains. Some un-reacted 'particles' are present in a wider reacted band, which is closer to the external surface of the grain, and can be observed in Fig. 11 a).

The purpose of the Fig. 11 data set was to determine the approximate resolution limit that this particular system configuration would allow, hence the choice of a structure that exhibited such fine detail. The scale bars illustrated in a) and b) show that the grain is of average size, measuring about 25 μm at the widest 2D dimension. The data set was captured with a digital zoom factor of ×5 that brought the total magnification to ×3150, and capture of the data was averaged over 4 scans per line to reduce noise. The data set was then processed with a simple low-pass filter, before being re-processed with an iterative deconvolution filter. This combination of filters did not appear to degrade the image and fine surface and structural features became better resolved as a result of removal of 'lens flare' and stray light.

Fig. 11 c) is an enlarged area of the top half of the grain shown in b), where a zoom factor of ×10 gives a total system magnification of ×6300. This image was also digitised to 1024 × 1024 pixels allowing better image clarity, whereas all the other confocal images presented are from 512 × 512 data sets. Very fine internal pore structures can be observed, an example of which has been measured with the confocal software as being approximately 0.17 μm across. It is possible to observe structures even smaller than this, but resolution of these features has been lost and their appearance is blurry.

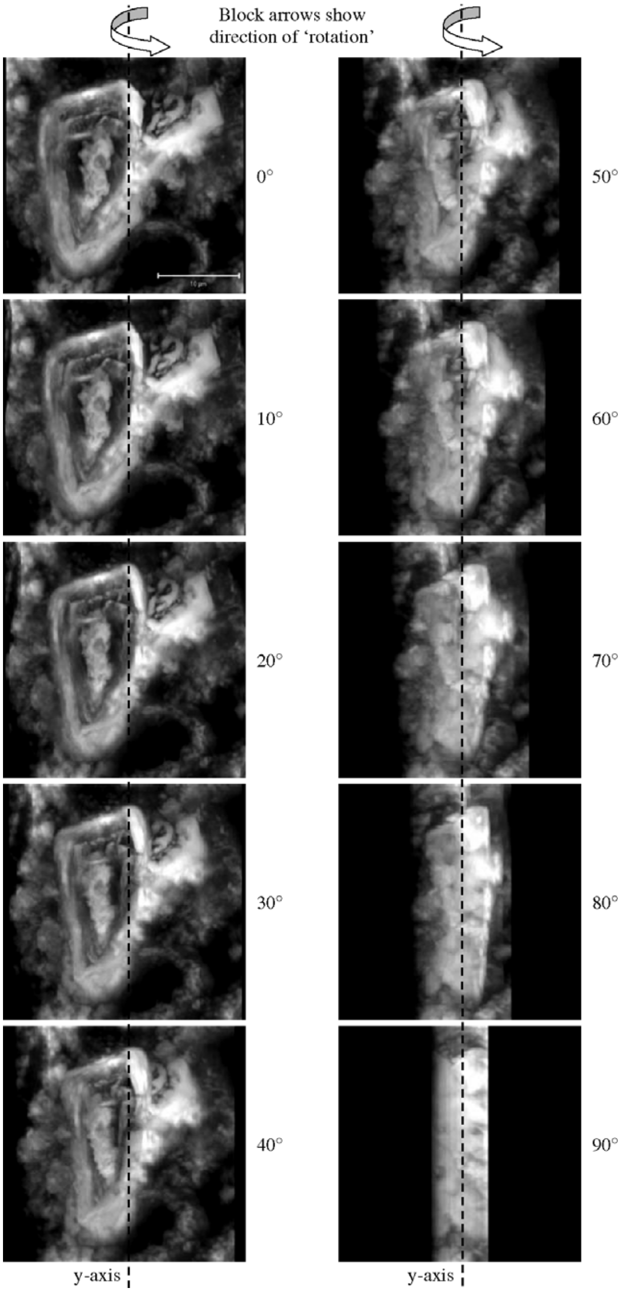

Fig. 12. 3D reconstruction of particle from Fig. 11 a). Reconstruction interval = 10° about y-axis (direction of rotation marked by arrows). Note: scale bar in first image = 10 μm.

The internal reacted features of the grain are perhaps best observed with a rotational virtual 3D model, which is illustrated in Fig. 12. The rotation of the model is anti-clockwise about the y-axis as viewed and shows that the finer internal banding of the reacted voids is not continuous, and is inclined to the plane of the section, although this is not readily observed on 2D images. The surface of the reacted core appears rough, but generally follows the overall morphology of the grain.

Note the faint banding in the final image of Fig. 12, which is due to the coarse overlap of 39 optical slices, which is fewer than would normally be captured during very high resolution imaging. The pinhole setting was about 0.3 AU that would normally require about 90 optical slices if the optical interval is optimised for best overlap. In this case image capture was averaged over 4 scans per line to help remove noise and to improve image feature resolution (at the image capture stage). If this was performed over ~90 slices, the time available for data capture would have been exceeded.

Fig. 13 is an image taken from the depth-compensated data set presented in Fig. 5 b). The image is actually number 11 in the z-stack and corresponds to a focal depth of 2.52 μm below the image stack surface (approximate vertical position of specimen surface). The magnification of this image is ×630, which is lower than the high resolution image shown in Fig. 11, but shows a variety of other features. The purpose of this image is to demonstrate that many different features can still be identified at depths below the surface, and are still able to be resolved at resolutions approaching that of an SEM.

Several fully or almost fully reacted cement grains can be observed, such as the clump of grains near the edge in the lower left quarter of the image, and the grain in the centre of the image. This grain displays a couple of 'black' areas that correspond to un-reacted phases/particles still present within the original grain boundary. In the lower left corner of the image a fine crack in the aggregate can be observed. Most of the aggregate particles are transparent grains of quartz, and cracks can be easily tracked through the body of the particle using this technique. A porous zone around the interface of an aggregate particle can be observed on the right edge of the image just below the centre line. In the centre of the top half of the image a large partly reacted grain is present. Very fine pore networks or structures appear to exist in most areas of the HCP. Some smaller particles appear to possess reacted rims or porous interfaces, or interface cracks that clearly delineate their shape. In standard fluorescent imaging modes, this detail is not resolved due to interference light emanating from adjacent out-of-focus x–y image planes.

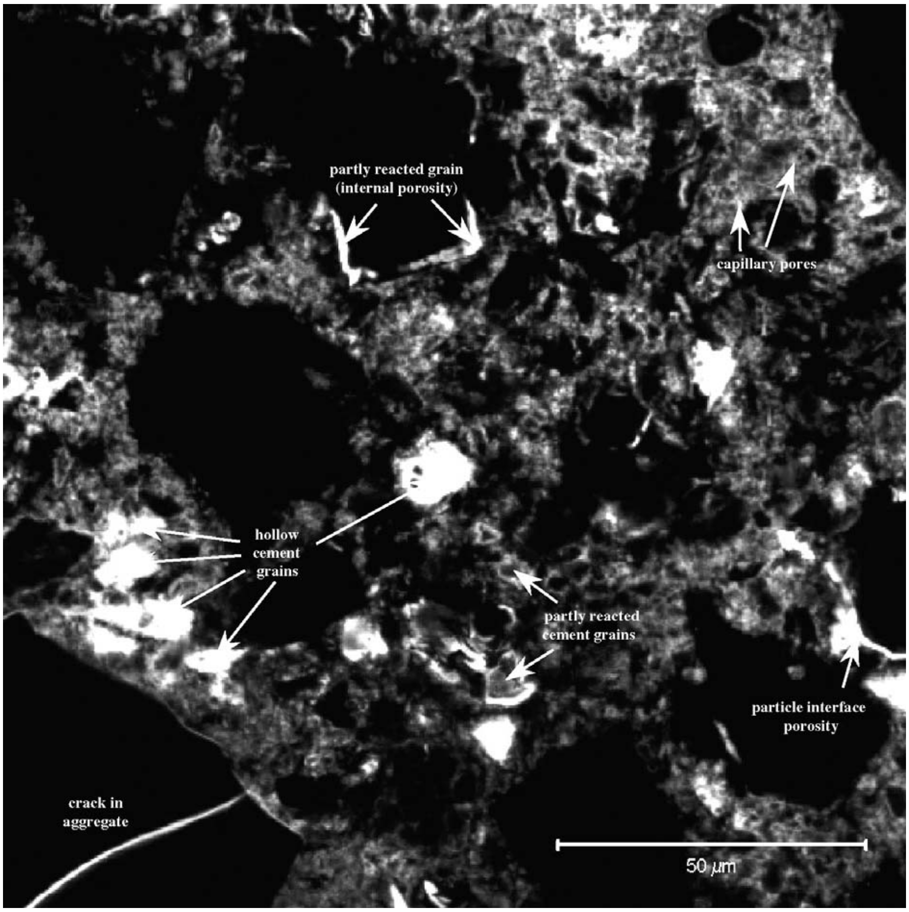

Fig. 13. Image of HCP porosity taken from data set shown in Fig. 5 b).

7. 3D model reconstruction and discussion

The ultimate aim of producing 3D image data is to construct virtual 3D models of image features that can be measured and analysed for geometry, connectivity, shape etc. The microscope's software is able to construct such models, which provide a general perspective and approximation of image data set physical dimensions. As image features *only* represent spaces that have been in-filled with fluorescent resin, image models formed by the computer on screen can be thought of as *virtual casts* of the inside of pores, voids or cracks, created by surface rendering of image data. Four of these models, which cover previous image figures, are presented in Fig. 14.

The models appear rough and idealised, which is consequential to differing levels of image resolution obtained during test image capture, and approximate selection of threshold values for image segmentation. When

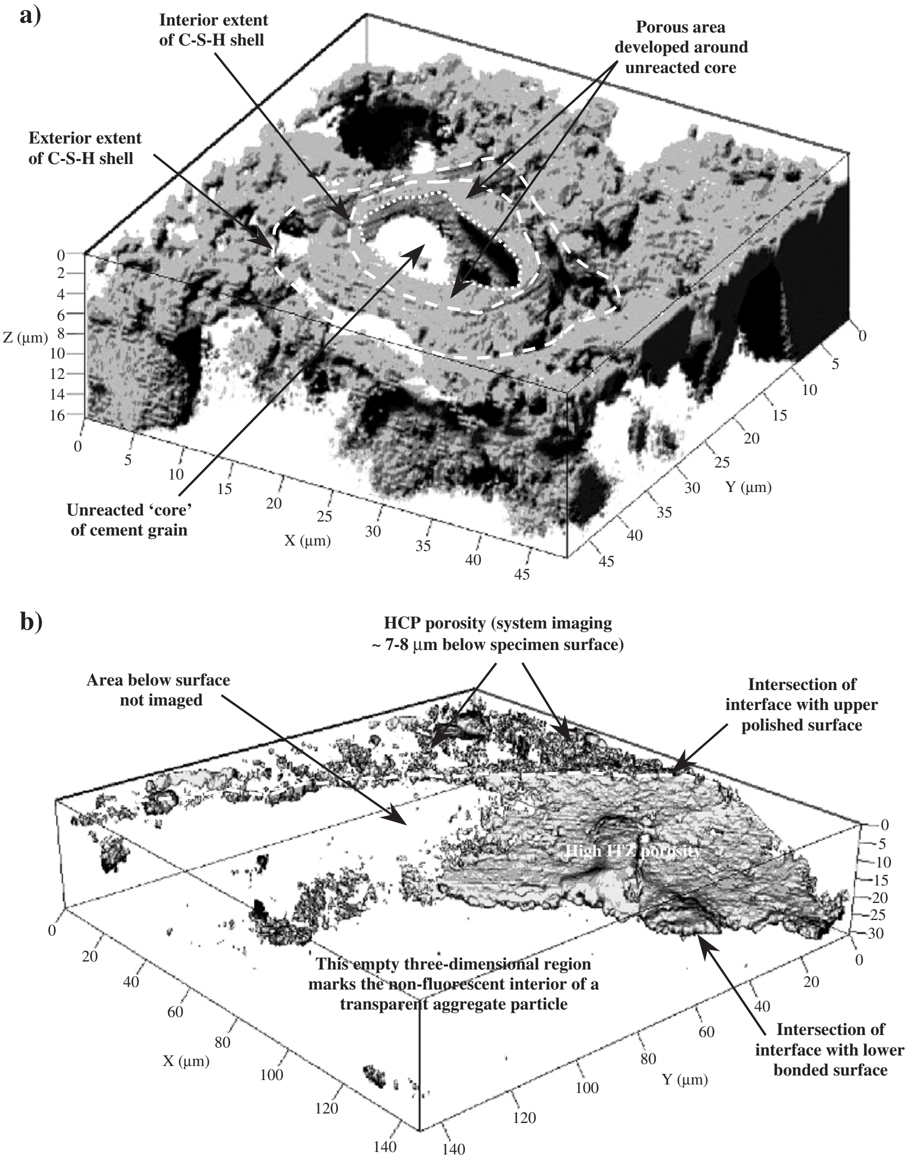

Fig. 14. Virtual 3D models of selected data sets. Each model bounded by a scaled sizing frame. a). Model of porosity associated with partially reacted cement grain shown in Fig. 9. Note: black areas due to shadow effect used to emphasise 3D features. Dashed lines mark approximate position of outer C–S–H shell intersection with specimen upper surface, inner dotted line marks approximate intersection of unreacted core with upper surface. b). Model of interfacial porosity around the quartz sand particle shown in Fig. 10. The vertical axis is scaled to approximately 30 μm which is the full thickness of the thin-section. The most prominent feature is the area of high ITZ porosity which occupies about half of the interfacial area shown in the reconstruction. Notice that some features present in Fig. 10 have been omitted (such as the crack in the aggregate), which is due to the 3D threshold values used. c). Model of porosity within partly reacted cement grain shown in Figs. 7, 11 and 12. Dashed white line marks approximate position of the non-reacted 'inner core' intersecting with the upper polished surface of the specimen. A reacted centre to the non-reacted core is however visible and is marked with a 'p'. Large blank areas around the pore structure indicate the presence of hydration (solid) products that were not impregnated by the fluorescent resin. d). Model of a random area of HCP showing partly reacted and fully reacted cement grain porosity, capillary pores, interfacial porosity and cracked aggregate particle described in Figs. 5 and 13.

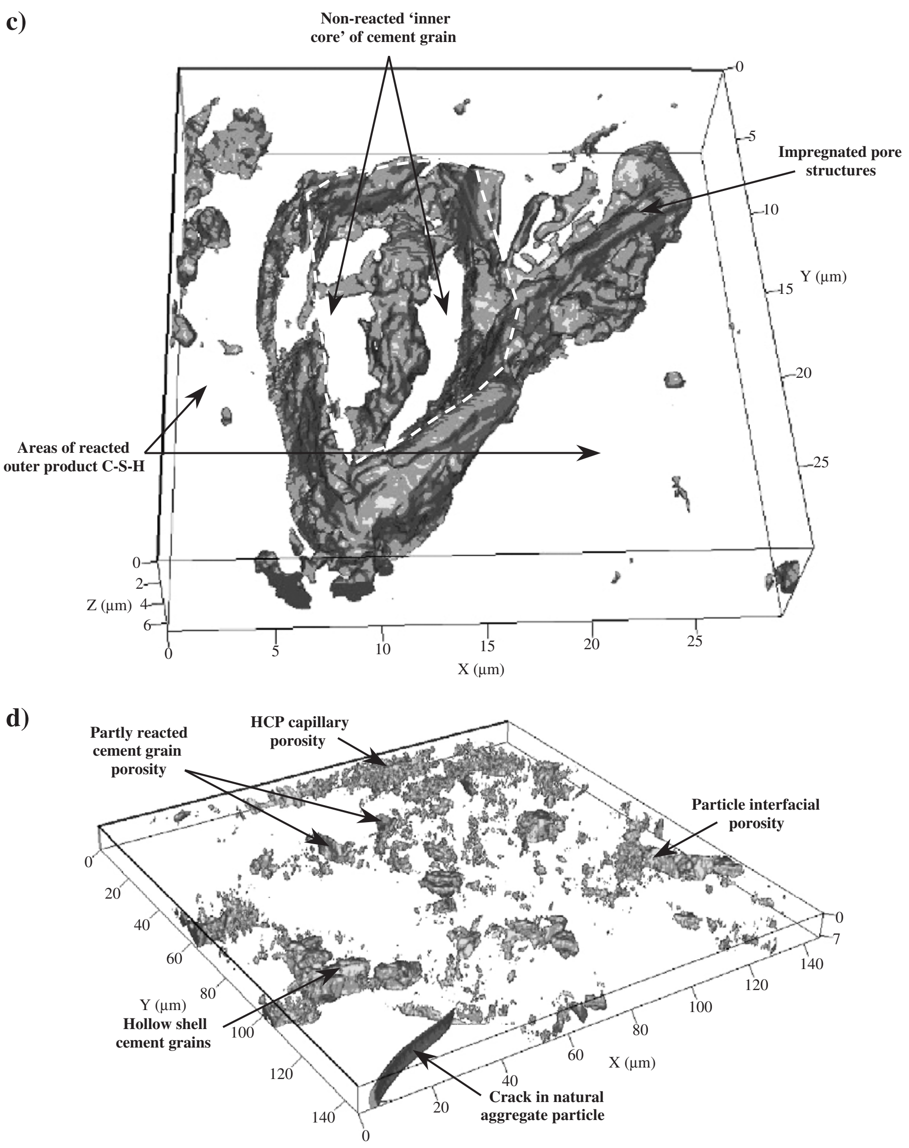

Fig. 14 (*continued*).

image capture is perfected the models will be input to specialist 3D image manipulation software, where they can be more accurately thresholded based on 3D densitometric criteria. To characterise the models, measurement algorithms and routines are being developed for reconstruction, measurement and image quantification.

Fig. 14 a) is a virtual 3D reconstruction of Fig. 9. This data set presented a partly reacted cement grain that was connected to capillary porosity by a connecting 'neck'. The neck is not visible in the orientation of the model as shown, being obscured by an area of capillary porosity outside of the grain. Different fractions of the grain have been marked to show the un-reacted core, the impregnated porous zone around the core, and the dense outer shell of C–S–H. Some linearity of data can be observed in different parts of the image, which is caused by the relatively coarse optical and *z*-axis resolutions used to capture this experimental data set. This also explains the blurry appearance of the model and rather fuzzy appearance of the image gallery shown in Fig. 9. The apparent suitability of fluorescent LSCM to the 3D studies of partially or fully reacted cement grains is a significant finding of the work.

Imaging of transparent natural aggregate (quartz sand) interfaces has also proved possible, as was first suggested by Kurtis et al. [7] from their study of glass bead interfaces, and Collins et al. [8] from follow-up studies of alkali–silica reactions using confocal reflected light techniques. Fig. 14 b) shows the 3D model created for the aggregate interface presented in Fig. 10. This was captured at a slightly higher optical resolution, but still shows evidence of linear features within the area of 'high ITZ porosity'. The model clearly shows the concave nature of the aggregate interface, and that very low levels of porosity exist in the blank interfacial region (to the left as viewed in Fig. 14 b)). The most important feature to note in this model however is the high ITZ porosity, which occupies half of the imaged interface, and is well connected to HCP porosity. This also provides evidence for the non-continuous nature of ITZ porosity around a particle of natural aggregate implying that the ITZ is variable, in terms of measured porosity, with some areas that are highly porous and other areas that are not. These findings have clear implications for modelling of the ITZ using idealised structures such as overlapping spheres etc.

Features observed through the aggregate/paste interface can be measured with a similar degree of accuracy, as features measured on the surface. Undoubtedly, when imaging through much thicker volumes of quartz, or quartz which is semi-transparent (translucent) or even discoloured due to the inclusion of elements such as manganese or ferric iron (amethyst), or manganese or titanium (rose quartz), the optical properties of the material may be much reduced. However with the confocal technique, imaging through a few 10s of micro-meters is unlikely to cause a severe limiting of the systems' ability to form a useful image. As the majority of natural aggregates contain transparent or semi-transparent minerals in greater proportions than opaque or light absorbing minerals, it is felt that the ability to analyse field concrete would not be severely affected, but it is likely that some minor instances could arise.

Fig. 14 c) is a 3D reconstruction of the highest resolution data set (Figs. 7, 11 and 12) captured for a partly reacted cement grain, and has formed the focus of on-going work to construct and segment 3D data. The partly reacted grain can be seen to have a largely un-reacted core, but the very centre of the core has reacted to form a pore space marked 'p'. The intersection of the unreacted core with the specimen surface has been marked by a dashed line.

Fig. 14 d) is the final 3D model produced, and shows a random area of HCP extracted from the data set presented in Figs. 5 and 13. The depth imaged was just over 7 μm and a variety of impregnated pore features can be observed. This model is arguably the most important of the four, as it represents a random area of HCP, and as such represents the majority of the hardened concrete excluding the aggregate. The amount and connectivity of HCP capillary pores contained within this fraction of the material, is likely to be the factor controlling transport related properties.

A major advantage of the confocal technique over conventional optical microscopy is the improvement in 2D lateral resolution. Fine structural detail is clearly imaged thanks to the introduction of the pinhole aperture, which blocks out-of-focus light from entering the detector and has the effect of reducing the thickness of the imaging plane (optical slice) to approximately 0.3 μm. Spatial resolution in transmitted white light is largely limited by the thickness of the specimen, and reflected white light is limited to imaging of the surface only, with relatively poor contrast levels.

The main appeal with confocal imaging however, is its ability to image through the z-axis as well as in the $x-y$ plane to give 3D image data, although loss of signal due to non-penetration of the beam and dispersion of emitted light with increased depth into the HCP was observed. The depth of material that can be probed by the laser is limited due to the very fine grain structure of HCP. It was found though, that the loss of signal with depth could be compensated for, by adjusting the laser probe and detector sensitivity. We have determined that if suitable adjustments are made to the detector sensitivity, depths of ∼12 μm below the specimen surface can be imaged without significant loss of resolution. Probed depths are smaller than other comparable 3D techniques such as x-rays and synchrotron radiation, but the resolution is similar or better and imaging is generally less costly.

Other limitations of the technique include the need to dry and impregnate specimens with fluorescent resin prior to data collection, which unless great care is taken, leads to micro-structural damage. Specimens also need to be polished to a very high surface finish to maximise the efficiency of light rays as they pass through transparent/translucent particles on their way to and from the target area. Here the surface of the HCP was monitored to obtain the best finish, resulting in a compromise in the level of damage remaining on aggregate surfaces whereas other techniques, such as high-energy x-ray sources, can probe specimens that do not require such a high level of preparation.

8. Conclusions

The objectives of the work were to establish whether fluorescent LSCM could be used to image the 3D pore structure of hardened cement-based materials, and to assess the depth of the material that could be probed. We have shown that the technique clearly works for imaging of very fine pores and voids, although more work is required to refine and quantify procedures. A number of different micro-pores and voids have been imaged at varying depths below the specimen surface, and we have shown how it is possible to use the more conventional technique of backscattered electron imaging to confirm the identity of features present in confocal images. We have established that the depth of useful signal penetration through the HCP is in the order of about 10 μm, but that this increases to at least the thickness of a thin-section (i.e., 25–30 μm) when imaging through transparent material. Imaging of hollow shell cement grains has revealed their connection to capillary pores, which will be examined further in subsequent work. High resolution imaging has allowed us to produce virtual 3D models, which forms a precursor to planned work to characterise the 3D structure, size and geometry of HCP pores and voids. Minimum resolution of structures has been identified at approximately 0.2 μm, with a similar resolution along the z-axis, and is comparable to that obtained with a scanning electron microscope.

Acknowledgements

The authors would like to acknowledge EPSRC for support under grant GR/M97206, and for equipment funding under grant GR/S18175. We would also like to thank Carl Zeiss UK Ltd for their help and advice with the LSM 510 confocal microscope and the loan of a specialist materials objective lens for image capture sessions, and the Department of Biochemistry at Imperial College London for access to their instrument. We would also like to thank Hong Seong Wong for valuable discussions during development of the image capture stages.

References

[1] N. Petford, G. Davidson, J.A. Miller, Pore structure determination using confocal scanning laser microscopy, Phys. Chem. Earth (A), vol. 24 (7), Elsevier Science Ltd., 1999, pp. 563–567.

[2] B. Menendez, C. David, A.M. Nistal, Confocal scanning laser microscopy applied to the study of pore and crack networks in rocks, Computers and Geosciences, vol. 27, Elsevier Science Ltd., 2001, pp. 1101–1109.

[3] J.T. Fredrich, 3D imaging of porous media using laser scanning confocal microscopy with applications to microscale transport processes, Phys. Chem. Earth (A), vol. 24 (7), Elsevier Science Ltd., 1999, pp. 551–561.

[4] B. Menendez, C. David, M. Darot, A study of the crack network in thermally and mechanically cracked granite samples using confocal scanning laser microscopy, Phys. Chem. Earth (A), vol. 27 (7), Elsevier Science Ltd., 1999, pp. 627–632.

[5] D.A. Lange, H.M. Jennings, S.P. Shah, Analysis of surface roughness using confocal microscopy, Journal of Materials Science, vol. 28 (14), Chapman & Hall, 1993, pp. 3879–3884.

[6] B. Walk-Lauffer, R. Bornemann, D. Knöfel, E. Thiel, In situ observation of hydrating cement-clinker phases by means of confocal scanning microscopy — first results, 24th International Congress on Cement Microscopy, 2002, pp. 95–106.

[7] K.E. Kurtis, N.B. El-Askar, C.L. Collins, N.N. Naik, Examining cement-based material by laser scanning confocal microscopy, Cement and Concrete Composites, vol. 25 (7), Elsevier Science Ltd., 2003, pp. 695–701.

[8] C.L. Collins, J.H. Ideker, K.E. Kurtis, Laser scanning confocal microscopy for in situ monitoring of alkali–silica reaction, Journal of Microscopy, vol. 213 (2), The Royal Microscopical Society, 2004, pp. 149–157.

[9] H.N. Walker, B.F. Marshall, Methods and equipment used in preparing and examining fluorescent ultrathin sections of Portland cement, Cement, Concrete, and Aggregates, vol. 1 (1), ASTM, 1979, pp. 3–9. CCAGDP.

[10] K.L. Gardner, Impregnation technique using coloured epoxy to define porosity in petrographic thin sections, Can. J. Earth Sci. 17 (1980) 1104–1107.

[11] B. Mayfield, The quantitative evaluation of the water/cement ratio using fluorescence microscopy, Mag. Concr. Res. 42 (150) (1990) 45–49.

[12] U.H. Jakobsen, V. Johanssen, N. Thaulow, Estimating the capillary porosity of cement paste by fluorescence microscopy and image analysis, Mat. Res. Soc. Symp., vol. 370, Materials Research Society, 1995, pp. 227–236.

[13] L. Elsen, N. Lens, T. Aarre, D. Quenard, V. Smolej, Determination of the W/C ratio of hardened cement paste and concrete samples on thin sections using automated image analysis techniques, Cement and Concrete Research, vol. 25 (4), Elsevier Science Ltd., 1995, pp. 827–834.

[14] J.A. Larbi, W.M.M. Heijnen, Determination of the cement content of five samples of hardened concrete by means of optical microscopy, Heron 42 (2) (1997) 125–138.

[15] J.B. de Monvel, E. Scarfone, S. Le Calvez, M. Ulfendahl, Image-adaptive deconvolution for three-dimensional deep biological imaging, Biophysical Journal, vol. 85 (6), Biophysical Society, 2003, pp. 3991–4001.